Evaluation of Wildfire Plume Injection Heights Estimated from Operational Weather Radar Observations using Airborne Lidar Retrievals

Enter authors here: M. Krishna[1,2], P. E. Saide[1,3], X. Ye[1,4], F. Turney[1], J. W. Hair[5], M. Fenn[5] and T. Shingler[5]

[1]Department of Atmospheric and Oceanic Sciences, University of California—Los Angeles, CA, USA

[2]Department of Earth Sciences, Dartmouth College, Hanover, NH, USA

[3]Institute of the Environment and Sustainability, University of California—Los Angeles, CA, USA

[4]Institute of Urban Environment, Chinese Academy of Sciences, Xiamen, China

[5]NASA Langley Research Center, Hampton, VA, USA

Corresponding authors: Mansa Krishna (mansakrishna23@ucla.edu), Pablo E. Saide (saide@atmos.ucla.edu)

Key Points:

- Weather radar estimates of biomass burning debris injection heights are evaluated against aerosol heights from airborne lidar.
- Radar maximum injection heights tend to be overpredicted while mean, median, 75th and 90th percentiles perform better.
- The maximum injection height can be predicted generally well by the 75th to 90th percentiles of the radar estimates.

Abstract

The vertical distribution of wildfire smoke aerosols is important in determining its environmental impacts but existing observations of smoke heights generally do not possess the temporal resolution required to fully resolve the diurnal behavior of wildfire smoke injection. We use Weather Surveillance Radar-1988 Doppler (WSR-88D) dual polarization data to estimate injection heights of Biomass Burning Debris (BBD) generated by fires. We detect BBD as a surrogate for smoke aerosols, which are often collocated with BBD near the fire but are not within the size range detectable by these radars. Injection heights of BBD are derived for 2-10 August 2019, using radar reflectivity ($Z \geq 10$ dBZ) and dual polarization correlation coefficients ($0.2 < C.C < 0.9$) to study the Williams Flats Fire event. Results show the expected diurnal cycles with maximum injection heights present during the late afternoon period when the fire's intensity and convective mixing are maximized. Radar and airborne lidar injection height comparisons reveal that this method is sensitive to outliers and generally overpredicts maximum heights by 40%, though mean and median heights are better captured (<20% mean error). Radar heights between the 75th and 90th percentile seem to accurately represent the maximum, with the exception of heights estimated during the occurrence of pyro-cumulonimbus. Location specific mapping of radar and lidar injection heights reveal that they diverge further away from the fire due to BBD settling. Most importantly, radar-derived injection height estimates provide near continuous smoke height information, allowing for the study of diurnal variability of smoke injections.

Plain Language Summary

Wildfire smoke aerosols injected into the atmosphere pose a serious threat to human health and the environment. Once in the atmosphere, aerosols travel long distances and affect air quality in regions much farther away. These 'long distances' are strongly correlated with the maximum heights aerosols can reach near their source, making it important to observe these 'injection heights'. However, existing observations of injection heights are limited temporally, making it difficult to study their diurnal and day-to-day variability. Here, we use weather radar data to estimate injection heights of Biomass Burning Debris (BBD), which is assumed to be collocated with aerosols that are too small to be detected by radars. Injection heights are estimated for the Williams Flats Fire event in Washington for 2-10 August 2019. Results show that daily

maximum injection heights occur in the late afternoon, when the wildfire's intensity is strongest. Further, radar-derived heights are compared to airborne lidar-derived heights for the same fire, revealing that the maximums are overpredicted but intermediate values like the mean are well represented. Radar-derived injection height estimates allow for near continuous smoke heights, making it relevant for future studies.

1 Introduction

The issue of air quality is a pressing concern due to the rapidly developing global economy and increased industrialization and urbanization (Manisalidis et al., 2020). Not only is the deterioration of air quality significant due to its environmental and ecological impacts, but also due to the health risk it poses for humans (Gakidou et al., 2017). Wildfires contribute to this burden on human health by emitting smoke aerosols into the atmosphere (Balmes, 2020), which is a rising concern as the number of catastrophic wildfires worldwide are increasing with climate change (Deb et al., 2020; Higuera & Abatzoglou, 2021). Furthermore, wildfire smoke aerosols injected into the atmosphere above the boundary layer can travel long distances and affect surface air quality in downwind regions (Buchholz et al., 2022; Hung et al., 2020). The injection heights of these aerosols in the atmosphere are closely related to the residence time of aerosols in the atmosphere and the distance they are transported (Schum et al., 2018), implying that greater injection heights could lead to more widespread impacts on air quality, making it important to better observe the vertical distribution of these smoke aerosols.

According to prior studies, smoke injection heights have been estimated in multiple ways. Multiple space-based estimation techniques exist, including the vertical profiles of aerosol and cloud backscatter provided by the Cloud-Aerosol Lidar with Orthogonal Polarization (CALIOP) instrument (Amiridis et al., 2010; Winker et al., 2004) and using the smoke height products retrieved from various passive remote sensing instruments such as the Multi-angle Imaging SpectroRadiometer (MISR) (M. Val Martin et al., 2010; Maria Val Martin et al., 2018), the Tropospheric Monitoring Instrument (TROPOMI) (Chen et al., 2021; Michailidis et al., 2022; Veefkind et al., 2012), the Moderate Resolution Imaging Spectroradiometer (MODIS), and the Visible Infrared Imaging Radiometer Suite (VIIRS) (Hsu et al., 2019; Lee et al., 2015; Loría-Salazar et al., 2021; Sayer et al., 2019). However, these retrievals are limited by the fact that the sun-synchronous orbits of all these satellites only allow for one or two overpasses in a given day

(Maria Val Martin et al., 2018). Though stereo imaging from a pair of geostationary (GEO) satellites with overlapping coverage is able to overcome the aforementioned limitation, this method has not been extensively validated and is only available during the daytime (Carr et al., 2020; Hasler, 1981). Thus, there is a need to develop and evaluate smoke injection height estimates that cover full diurnal cycles and have the potential to provide real-time measurements.

Here, we explore the use of the weather surveillance radar, an under-utilized tool for studying wildfires (McCarthy et al., 2019). Since smoke aerosols are often collocated with lofted debris in the vicinity of the fire, the radar can be used to retrieve the injection heights of Biomass Burning Debris (BBD) produced from wildfires as a possible surrogate for the injection heights of smoke aerosol plumes (Jones & Christopher, 2009). The significance of this approach lies in the fact that it posseses adequate spatial and temporal coverage and allows for the retrieval of a complete time series of plume injection heights and depicts day-to-day variability of the same (Jones & Christopher, 2009). While radar estimates of wildfire plume structure are being used to evaluate models (Shamsaei et al., 2023), they have not been thoroughly compared to more established observations of smoke plume height. Drawing inspiration from Jones & Christopher (2009), who have previously provided injection heights with an hourly resolution over a 2-day period, we retrieved plume injection heights for the whole lifetime of a fire and performed an evaluation of these retrievals. In the following study, we describe the methods used to derive smoke injection heights from radars, show results for the 2019 Williams Flats Fire, and evaluate them using airborne lidar data from the Fire Influence on Regional to Global Environments and Air Quality (FIREX-AQ) field campaign (Warneke et al., 2023). Conclusions and future directions are outlined in the sections to follow.

2 Data and methods

2.1 Weather Surveillance Radar-1988 Doppler (WSR-88D)

The WSR-88D network spread through the United States currently consists of 160 S-Band (10 cm) precipitation radars operated by the National Oceanic and Atmospheric Administration National Weather Service (Crum & Alberty, 1993; Holleman et al., 2022). Doppler Radars in the WSR-88D network alternate between two modes (i.e., clear-air mode and precipitation mode) and characterize echoes through reflectivity, correlation coefficient, radial velocity, and spectrum width, i.e., the base radar products (Crum & Alberty, 1993). In either

clear-air and precipitation mode, the radar is operated in one of many Volume Coverage Patterns (VCPs), which consists of the radar antenna making a series of 360° scans of the surrounding atmosphere for pre-determined, increasing elevation angles (Crum & Alberty, 1993; Kingfield & French, 2022; NOAA National Weather Service et al., 2023).

The localized instability and increased buoyancy produced by the heat of the fire may result in lofting of significant amounts of debris, ash, and other particulate matter several kilometers into the atmosphere (Kingsmill et al., 2023; Rodriguez et al., 2020; Thurston et al., 2017). It is important to note that the Doppler Radar is not sensitive to smoke particles (diameter $D < 100\ \mu$m), rather they are sensitive to BBD (diameter $D > 1$ mm) that are large enough to be detected by the weather radars (Banta et al., 1992; McCarthy et al., 2019).

2.2 Data collected: reflectivity and correlation coefficient characteristics

To estimate the plume injection heights of BBD for the 2019 Williams Flats Fire event in northeast Washington, ~216 hours of data was obtained (from 00:04:38 on 2 August 2019 to 00:04:47 on 11 August 2019) of Level II WSR-88D data from Doppler Radar KOTX (DOC/NOAA/NWS/ROC, 1991), which is approximately 80 km from the fire. During this period, the Doppler Radar operated in two modes: VCP-35 (clear-air mode) and VCP-215 (precipitation mode). When operated in VCP-35, radar data is collected at 9 elevation angles (0.5°, 0.9°, 1.3°, 1.8°, 2.4°, 3.1°, 4.0°, 5.1°, and 6.4°) approximately every 7 minutes, whereas in VCP-215, data is collected for 15 elevation angles (VCP-35 angles, 8.0°, 10.0°, 12.0°, 14.0°, 16.7°, and 19.5°) approximately every 6 minutes (NOAA National Weather Service et al., 2023).

The WSR-88D is designed to detect atmospheric targets or precipitation-sized hydrometeors (diameter $D > 100\ \mu$m) from backscattered electromagnetic energy in the microwave spectrum and the returned energy is used to determine the reflectivity (measured in dBZ) (Donald Burgess & Peter S. Ray, 1986). The Doppler Radar is also designed to detect how similarly the horizontally and vertically polarized pulses (of returned energy) are behaving; this similarity is quantified using the correlation coefficient (Doviak et al., 2000). Atmospheric targets that are highly variable in size and shape (such as debris or birds) will likely have less similarly behaving horizontal and vertical pulses, leading to lower correlation coefficient values (Melnikov et al., 2008; Zrnic et al., 2020); targets that are more uniform in size and shape (such

as rain droplets or snow) will have more similarly behaving horizontal and vertical pulses, leading to higher correlation coefficient values (Liu & Chandrasekar, 2000).

Radar reflectivity and correlation coefficient data were passed through the injection height estimation algorithm (details provided in Section 2.3) and hence used to estimate the injection heights of smoke aerosols.

2.3 Injection height estimation algorithm

The following injection height estimation algorithm uses Py-ART, a Python module developed for parsing weather radar data (Helmus & Collis, 2016). The radar data (i.e., the reflectivity and correlation coefficient data) was re-gridded into cartesian coordinates using Py-ART and then passed through the injection height estimation algorithm developed for this study. The algorithm works by analyzing a pre-determined, three-dimensional grid around a fire. Here, we studied the 2019 Williams Flats Fire (located at 47.98°N latitude, -118.624°E longitude) (Peterson et al., 2022; Ye et al., 2021, 2022), with the pre-determined grid defined to extend from 47.85°N to 48.05°N latitude and -118.70°E to -118.20°E longitude. The horizontal grid spacing is considered to be ~1000 m, similar to the range resolution described in National Research Council (2002). The radar vertical resolution can be approximated by the difference between the height of the center of the beams at consecutive angles, which at 80 km distance is 500-700m for the first four angles (0-2.5 km altitude) and increases from there (e.g., ~1 km resolution at ~4 km altitude, ~2 km resolution at 9-11 km altitude). Thus, the vertical resolution of the grid was set 500 m to get the most the radar vertical resolution at the lower levels. At each timestamp, the algorithm searches for vertical regions of continguous reflectivity exceeding or equal to a defined minimum reflectivity threshold, returning the maximum injection height if the reflectivity value falls below the minimum threshold (Figure 1a). For each (x, y) position within

the pre-determined grid, the algorithm can search up to a height of 14727 m in 500 m increments (Note that the height of the radar is 727 m above sea level).

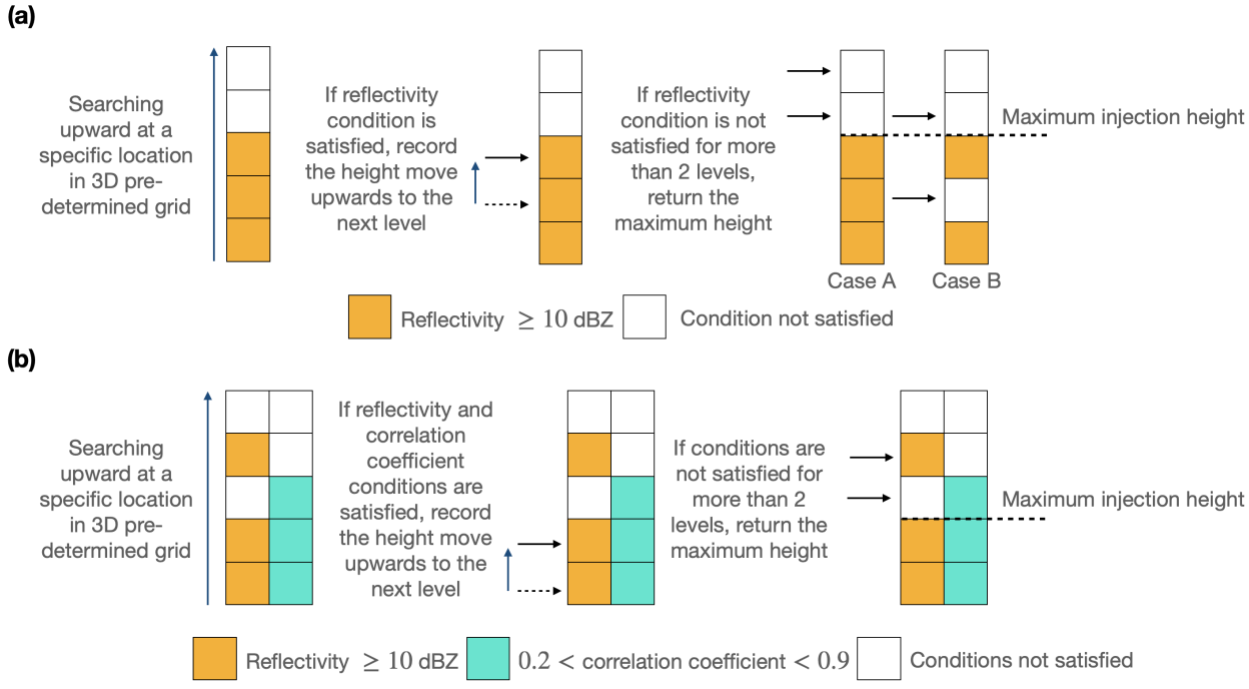

Figure 1. **Upper panel (a):** Diagrammatic representation of initial version of the injection height estimation algorithm. (Left) The algorithm searches upwards for each grid square within the pre-determined grid for regions of contiguous reflectivity, (Middle) the algorithm searches upwards iteratively if the current region satisfies the reflectivity threshold, (Right) the algorithm returns the last height for which the reflectivity threshold was satisfied if 2 'bad' reflectivity values are retrieved. The algorithm allows a buffer of 2 'bad' reflectivity values before retrieving the maximum height; case A depicts a contiguous reflectivity situation whereas case B depicts a (likely rare) discontiguous reflectivity situation. **Lower panel (b):** Similar to **(a)** but for the modified version of the injection height estimation algorithm. (Left) For each grid square, the algorithm iteratively searches upwards, (Middle) moving upwards if the reflectivity and correlation coefficient conditions are satisfied. (Right) The algorithm allows a buffer of 2 'bad' reflectivity or correlation coefficient values before retrieving the maximum injection height.

In previous studies, scientists utilized polarimetric data to identify smoke plumes, observing reflectivity values on the range of 10-25 dBZ (Lang et al., 2014; Zrnic et al., 2020). Therefore, drawing inspiration from existing literature, reflectivity threshold values for lofted

debris were tested in a range of 5-20 dBZ (Figure 2a). We considered 10 dBZ to be an appropriate minimum threshold as a 5 dBZ threshold generated heights that likely did not correspond to the smoke top since fire activity was very low between 14-19 UTC and thresholds of 15 dBZ and 20 dBZ tended to produce significantly lower heights for the more active fire period after 20 UTC (Ye et al., 2021). The 10 dBZ threshold is also consistent with the assumptions made in previous work (Jones & Christopher, 2009).

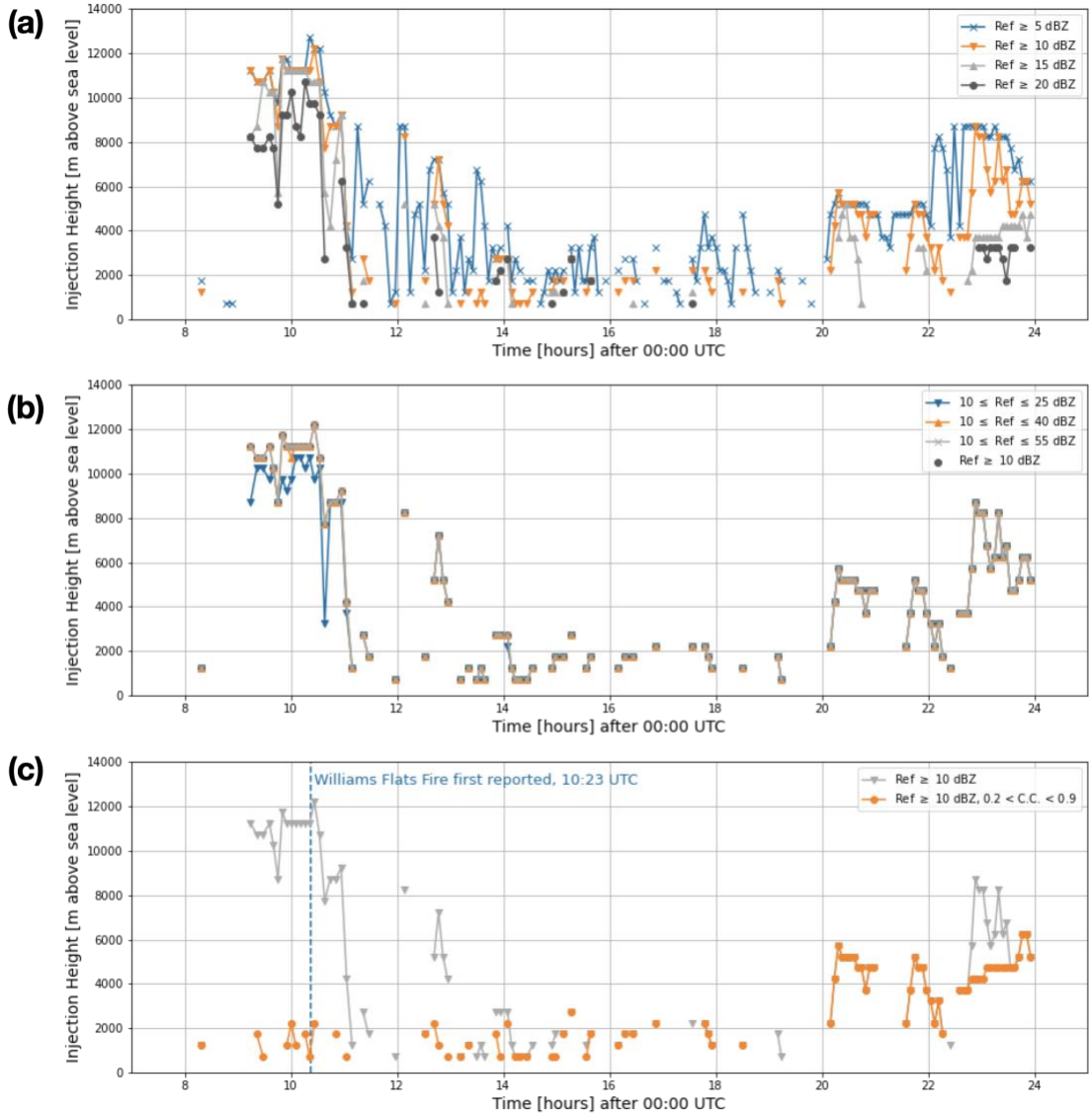

Figure 2. Injection heights estimated on 2 August 2019 (UTC). **(a)** Heights estimated using different lower bounds of reflectivity values: 5 dBZ, 10 dBZ, 15 dBZ, and 20 dBZ. The appropriate minimum threshold chosen was 10 dBZ. **(b)** Heights estimated using minimum

reflectivity threshold of 10 dBZ and different upper reflectivity thresholds: 25 dBZ, 40 dBZ, and 55 dBZ. **(c)** Initial (grey) and modified (orange) algorithms. The extremely high injection heights (upwards of 10 km above sea level) occur around the time the Williams Flats Fire began (dotted, blue vertical line), leading to the conclusion that the initial algorithm was likely picking up on the hydrometeors from the early-morning thunderstorm in the Colville Reservation, WA. The correlation coefficient constraint within the modified algorithm successfully reduces the heights retrieved.

The Williams Flats Fire, first reported at 10:23 UTC on 2 August 2019, was ignited by lightning strikes associated with the thunderstorm ~80 km northwest of the Doppler Radar (KOTX) (Ye et al., 2021). Therefore, the initial algorithm (Figure 1a) ran the risk of retrieving heights of atmospheric targets whose reflectivity exceeded the minimum threshold of 10 dBZ and were likely not BBD, but instead were more likely the hydrometeors present in the thunderstorm that initiated the fire. Attempts were made to discriminate between BBD and hydrometeors by setting an upper bound on the reflectivity values (Figure 2b), but this did not help in discriminating between BBD and the hydrometeors from the thunderstorm. Hence, other approaches were tested. A correlation coefficient constraint was embedded within the algorithm to curb the possible overestimation of injection heights; heights were only retrieved if both the reflectivity and correlation coefficient conditions were met to improve the injection height retrievals when rain or snow is present (Figure 1b). Based on existing literature, the correlation coefficient values inside smoke plumes tend to be below 0.8 (Melnikov et al., 2008; Zrnic et al., 2020) and rain or drizzle tends to have values above 0.9 (Liu & Chandrasekar, 2000), and thus a range of 0.2-0.9 was assumed for detecting BBD. Results from this modification are discussed in Sections 3 and 4. This modification proved to be effective in discerning between debris and hydrometeors as the injection heights retrieved for 2 August 2019 with the modified algorithm successfully eliminated the convective system (Figure 2c).

2.4 Datasets used as reference for evaluation

The Differential Absorption Lidar (DIAL) – High Spectral Resolution Lidar (HSRL) (Hair et al., 2018) from DC-8 aircraft during the FIREX-AQ field campaign was used as reference. The DC-8 sampled the Williams Flats Fire plume on 3, 6, and 7 August 2019 (PST), capturing multiple phases of the fire. Images of eleven transects overpassing the Williams Flats Fire on these days can be found in Ye et al. (2021). The DIAL-HSRL system is capable of

providing measurements of aerosol depolarization (355, 532, 1064 nm), aerosol/cloud extinction (532 nm), and backscatter coefficients (355, 532, 1064 nm) above and below flight height at a temporal resolution of 10 seconds. Maximum smoke injection heights were derived based on the vertical gradients of 532 nm backscatter coefficients, and are used in this study (Ye et al., 2021). It should be noted that while the lidar footprint is narrow, the measuring strategy implemented in FIREX-AQ consisted on doing an overpass at altitude across the axis of the plume, followed by several plume crossings at increasing distances downwind of the fire (Warneke et al., 2023). Since DIAL-HSRL detects aerosols that do not settle immediately (as is likely the case with BBD), the measurement strategy allows us to say with confidence that the retrieved heights are an accurate representation of the whole plume.

Geostationary satellite imagery produced specifically for FIREX-AQ by the Florida State University team was used to provide context regarding smoke and aircraft location (Warneke et al., 2023). Airborne lidar and satellite imagery are available in the FIREX-AQ data repository (NASA/LARC/SD/ASDC, 2020).

3 Results

3.1 Time series of injection heights

Using the injection height estimation algorithm (detailed in Section 2.3), an extended time series of the plume injection heights was retrieved for the 2019 Williams Flats Fire event (Figure 3). It should be noted that the time series captures the typical diurnal cycle of fires, with daily maximums occurring during the latter half of the day when the fire's intensity and convective mixing is maximized (Jones & Christopher, 2009; Zrnic et al., 2020). We also note that despite regular retrievals of radar data, there are visible gaps in the extended time series. This is likely due to the weak reflectivity observed during the morning period, as such we may conclude that the buoyancy flux of the fire was not strong enough to lift sufficient BBD to meet the reflectivity threshold or the correlation coefficient constraint (Rodriguez et al., 2020; Tory et al., 2018). The time series also shows large differences between intermediate heights (i.e., heights within the 25-75th percentile range) and the maximum heights during the most intense periods of the diurnal cycles, sometimes reaching >6 km differences, which needs to be further

assessed with reference observations.

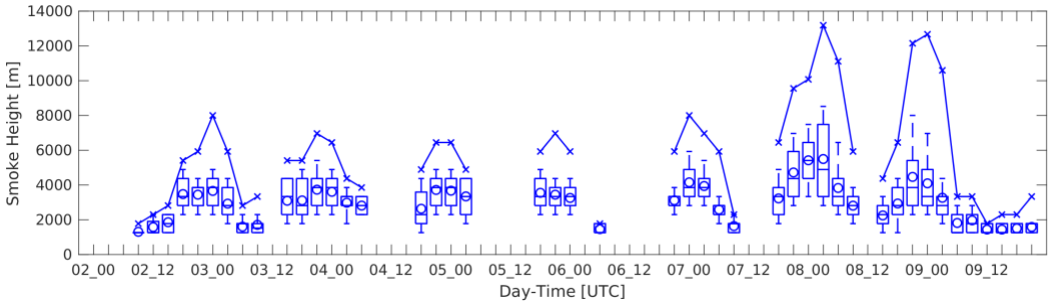

Figure 3. Box and whisker plots depicting an extended time series of radar-derived smoke injection heights (2-10 August 2019) aggregrated over 3-hour intervals. Central, solid lines indicate the median, circles indicate the mean, boxes indicate the lower and upper quartiles, whiskers indicate the upper and lower deciles, and the crosses connected with solid lines indicate the maximums. The time series captures the diurnal cycle of fires, displaying that the daily maximum injection heights are present during the late afternoon period. Visible gaps in the time series occur when the reflectivity and correlation coefficient conditions are not satisfied or when there were less than 10 samples in each time interval.

3.2 Comparison to injection heights retrieved from airborne lidar data

To evaluate the algorithm's accuracy in retrieving injection heights of BBD, they were compared to the injection heights derived from airborne lidar data from the 2019 FIREX-AQ campaign. The flight path of the aircraft (with the airborne lidar) tended to sample the whole extent of the plume, going beyond the pre-determined grid used to retrieve the radar-derived injection heights (the red box(es) in Figures 4a-c). Hence, the lidar-derived injection heights outside the pre-determined grid were removed for this comparison as BBD is expected to settle quickly and is therefore unlikely to match the smoke heights further away from the fire. Figure 5 shows distributions of injection heights for 3, 6, and 7 August 2019 (PST), which include the

days when the aircraft was sampling this fire.

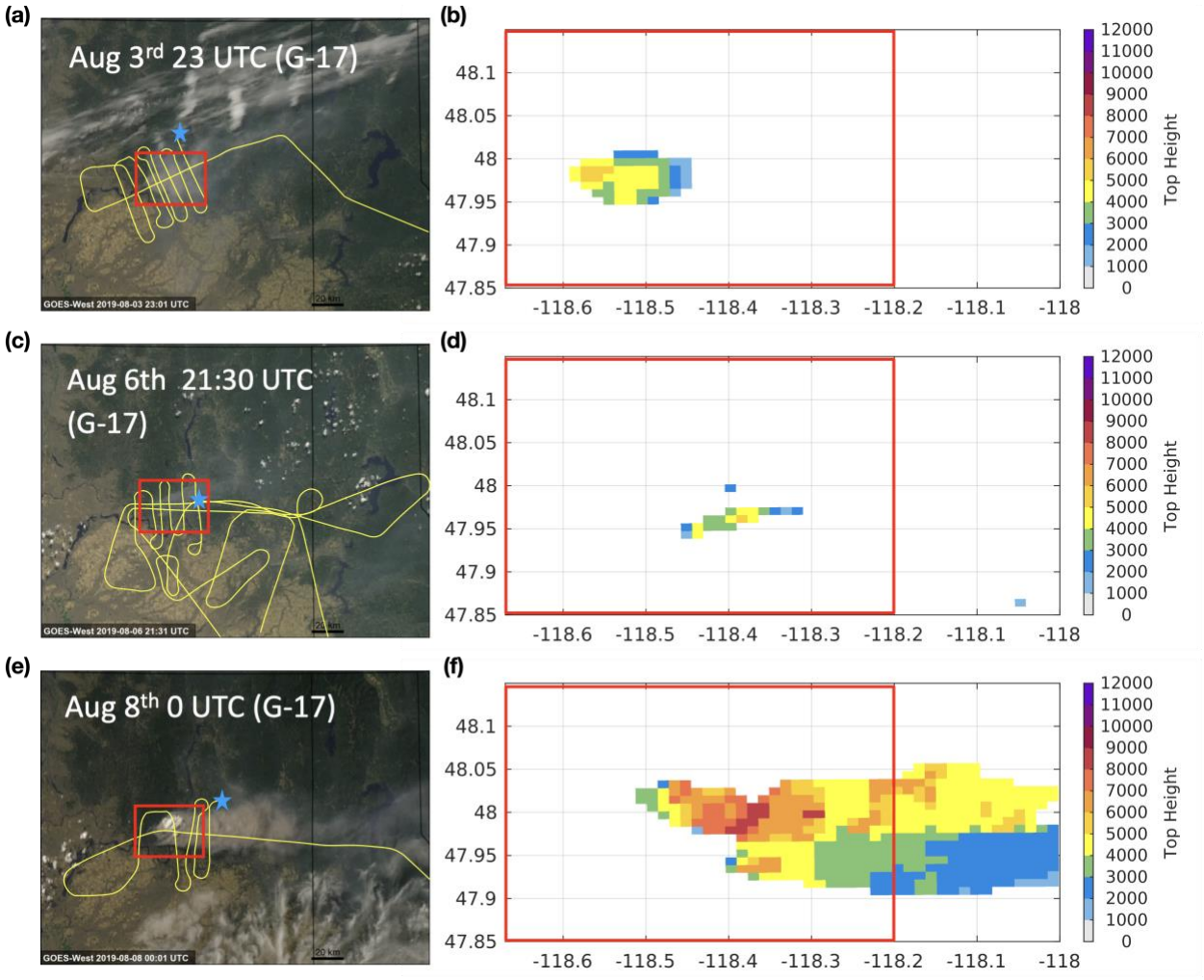

Figure 4. **Left panels (a) (c) (e):** FIREX-AQ flight paths (solid yellow lines) and pre-determined grid (red box) for flights on August 3, 6, and 7; Imagery from GOES-17 satellite imagery. The blue star represents the aircraft location at the time. **Right panels (b) (d) (f):** Maps of maximum injection heights derived from the radar data for the corresponding times.

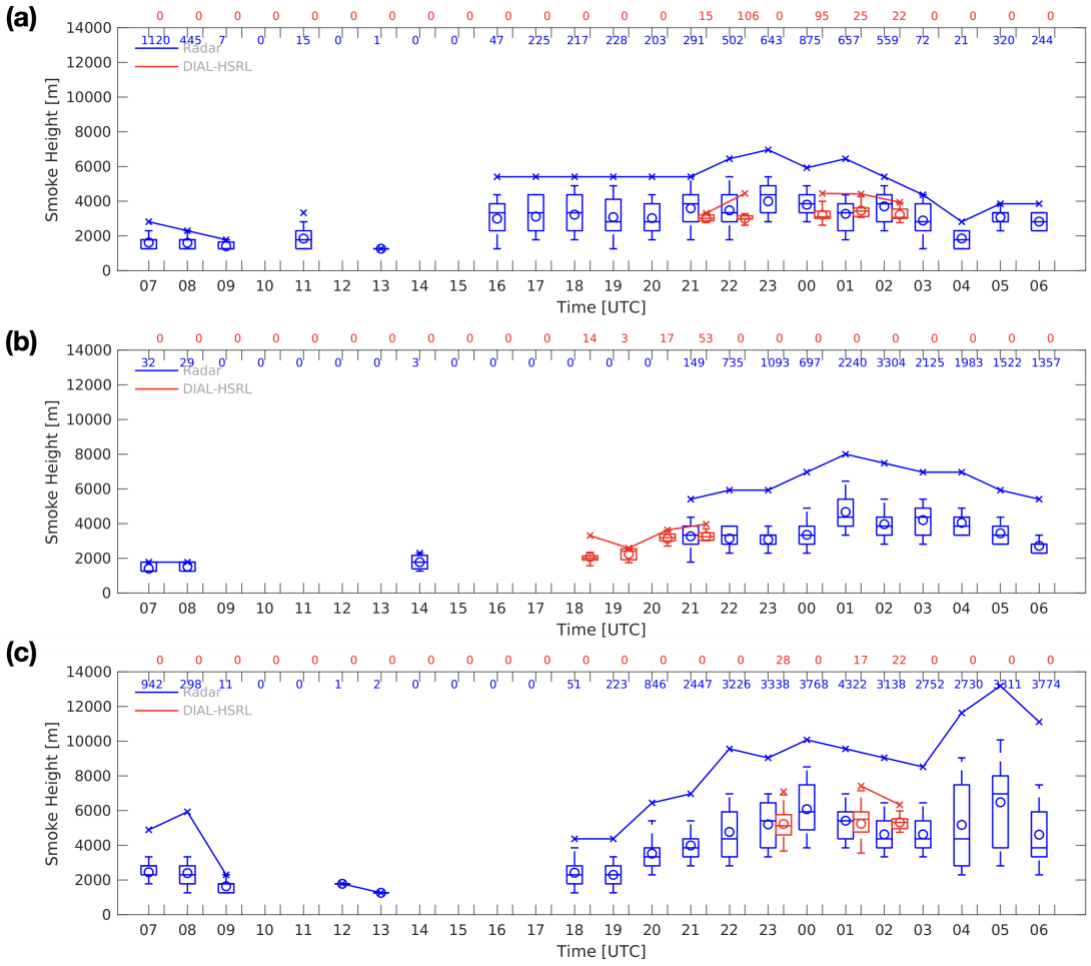

Figure 5. Box and whisker plots (similar to Figure 3) of the injection heights derived from both radar (blue) and airborne lidar (red) data for each hour (local time) on **(a)** 3 August 2019, **(b)** 6 August 2019, and **(c)** 7 August 2019. The number of data points for each hour is shown at the top of each panel, color-coded according to the corresponding box and whisker plot(s). For further details, see Table 1.

Table 1. Distribution of hourly maximum (R_{max}, L_{max}), mean (R_{mean}, L_{mean}), and median (R_{median}, L_{median}) injection heights derived from both radar and lidar data (in meters). The heights in the following table correspond to the maximum heights retrieved at the time the aircraft was airborne. Lidar-derived heights are retrieved according to the flight path and radar-derived heights are retrieved within the pre-determined grid. All values are rounded to 3 significant figures.

Date (PST)	Time (PST)	R_{max} (m)	L_{max} (m)	R_{mean} (m)	L_{mean} (m)	R_{median} (m)	L_{median} (m)	R_{75th_p} (m)	L_{75th_p} (m)	R_{90th_p} (m)	L_{90th_p} (m)
	14:00	5410	3310	3590	3020	3860	3010	4380	3220	5410	3310

3 Aug 2019	15:00	6450	4450	3480	3000	3340	3000	4380	3160	5410	3280
	17:00	5930	4450	3800	3220	3860	3100	4380	3420	4890	4000
	18:00	6450	4420	3280	3470	3340	3430	3860	3620	4380	4270
	19:00	5410	3940	3710	3230	3860	3070	4380	3550	4890	3910
6 Aug 2019	14:00	5410	3970	3270	3280	3340	3250	3860	3470	4380	3700
7 Aug 2019	16:00	9040	7090	5210	5230	5410	5130	6450	5770	6970	6890
	18:00	9560	7420	5420	5250	5410	5500	5930	5930	6970	6970
	19:00	9040	6340	4630	5330	4380	5320	5410	5530	6450	6040
Mean bias [m]		1920		151		221		596		820	
Mean % bias		40.0%		5.7%		8.5%		17.1%		22.7%	
Mean error [m]		1920		356		470		622		820	
Mean % error		40.0%		10.0%		13.3%		17.5%		22.7%	

From Figure 5, it can be concluded that the distribution of maximum injection heights derived from radar data is significantly wider than the injection heights derived from the lidar data. The maximum injection heights retrieved from the radar are overpredicted by ~2000 m, a 40% difference on average (Table 1). However, the mean, median, 75th and 90th percentiles seem to agree better with the injection heights derived from airborne lidar data (350-820 m mean error), though a general overprediction of heights persists (given the assumption that the airborne lidar data is the reference). Figure 5 also shows that the radar data is capable of capturing the increase in top injection heights from the 3rd and 6th of August to the 7th, thus capturing the day-to-day variability. As mentioned above, the time series of heights derived from radar data has gaps when fire intensity is not strong enough, but shallow smoke aerosol injections into the boundary layer could still occur during these periods (as seen during 18-20 UTC on 6 August 2019). On the other hand, each time free-tropospheric injections were detected by the lidar, the radar shows strong diurnal signals (Figure 5a, c). Thus, for applications using radar data to inject smoke into models, a fair assumption for injection when the radar signal is not available would be to place it within the boundary layer.

The overprediction by the injection height estimation algorithm (using radar data) could be occurring for several reasons. One potential reason for the overprediction is that the algorithm is retrieving maximum injection heights for each timestamp within the pre-determined grid whereas the lidar-derived injection heights are retrieved according to the flight path. Therefore, there is a possibility that the radar and lidar-derived injection heights are being retrieved for different locations. Hence, to make this comparison more robust, a location-specific injection height mapping was used. The injection heights were derived using the algorithm at the latitude-

longitude position of the aircraft. Reflectivity cross-sections over the flight track with the associated injection heights were plotted accordingly (Figure 6).

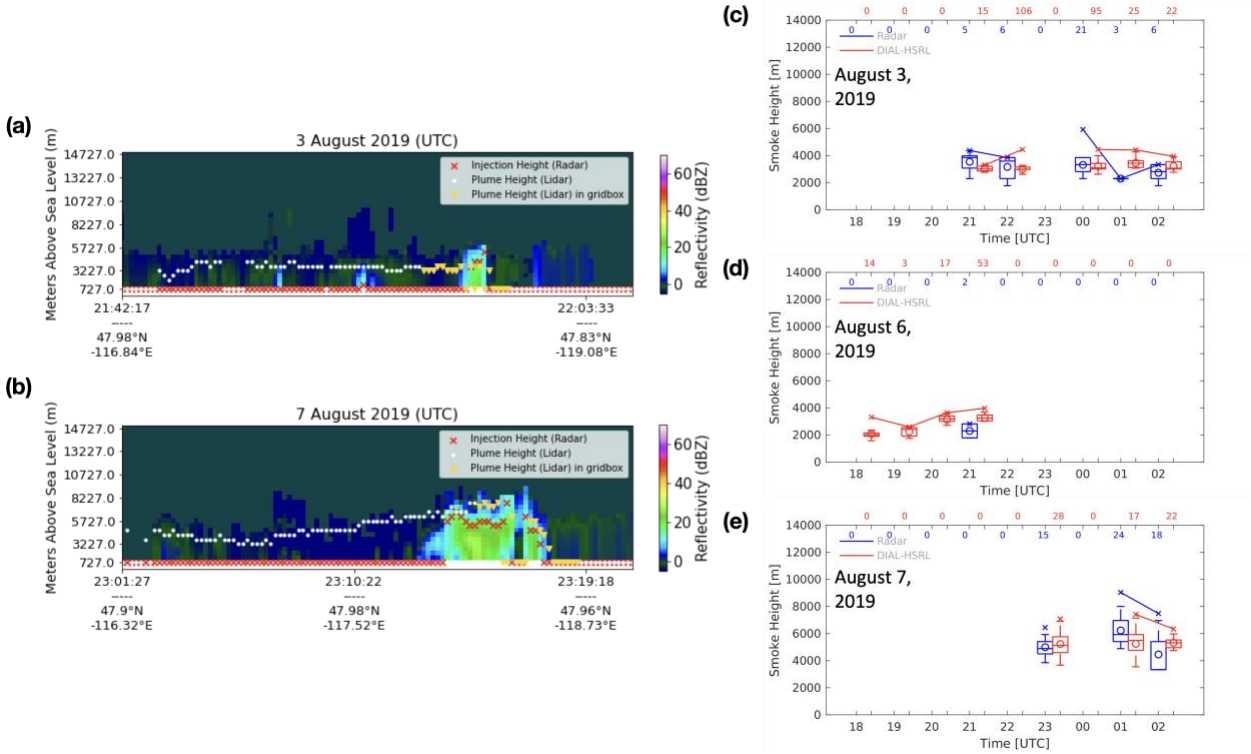

Figure 6. **Left panels:** Temporal cross-sections of reflectivity according to portions of the flight paths on **(a)** 3 August 2019 and **(b)** 7 August 2019. Injection heights are super-imposed on the cross-section. Radar derived injection heights are highlighted in red for both plots. Lidar-derived injection heights within the pre-determined grid are highlighted as yellow triangles. All other lidar-derived heights are shown as white dots. **Right panels:** Similar to Figure 5, but using radar data mapped according to the flight track instead for **(a)** 3 August 2019, **(b)** 6 August 2019, and **(c)** 7 August 2019.

Table 2. Further details on Figure 6. Similar to Table 1, but with radar data mapped according to the flight track for the appropriate days.

Date (PST)	Time (PST)	R_{max} (m)	L_{max} (m)	R_{mean} (m)	L_{mean} (m)	R_{median} (m)	L_{median} (m)	R_{75th_p} (m)	L_{75th_p} (m)	R_{90th_p} (m)	L_{90th_p} (m)
3 Aug 2019	14:00	4380	3310	3550	3020	3860	3010	3990	3220	4380	3310
	15:00	3860	4450	3170	3000	3600	3000	3860	3160	3860	3280
	17:00	5930	4450	3310	3220	3340	3100	3860	3420	4060	4000
	18:00	2300	4420	2300	3470	2300	3430	2300	3620	2300	4270
	19:00	3340	3940	2730	3230	2820	3070	3340	3550	3340	3910

6 Aug 2019	14:00	2820	3970	2300	3280	2300	3250	2820	3470	2820	3700
7 Aug 2019	16:00	6450	7090	5000	5230	4890	5130	5410	5770	5930	6890
	18:00	9040	7420	6230	5250	5930	5500	6970	5930	8110	6970
	19:00	7490	6340	4460	5330	3340	5320	5410	5530	6810	6040
Mean bias [m]		24.4		-220		-270		32.2		-84.4	
Mean % bias		-1.0%		-6.1%		-5.4%		0.8%		-2.0%	
Mean error [m]		1160		613		741		623		889	
Mean % error		24.4%		16.1%		19.6%		16.2%		19.9%	

After the location-specific mapping, we note that the maximum heights are much closer together within the pre-determined grid around the fire (Table 2), with the mean error dropping to 1160 m and near 0 bias. While bias is reduced, similar errors perist for other metrics (mean, median, and percentiles) (610-890 m). We also note that there are still some instances where the maximum injection height is largely overpredicted (e.g., 00 UTC on 4 August 2019, 01-02 UTC on 8 August 2019 in Figure 3). Previously mentioned in Section 2, the maximum injection heights for the whole domain should not substantially deviate from the lidar-derived injection heights due to the sampling strategy and the relatively low settling velocities of smoke aerosols. Thus, we hypothesize that the overprediction of maximum injection heights observed by the radar is due to outliers that are present throughout the time period of the fire. A reason for this could be the coarse vertical resolution of the radar which is 1-2 km for these heights (Section 2.3). Thus, using the mean, median, 75^{th} percentile, and 90^{th} percentile heights appears to be a more reliable use of radar data as resulting errors and biases are well within the expected radar resolution.

Figure 6 also shows that BBD (which is much larger and heavier than other intermediate particles) is settling or sinking much faster as opposed to the smoke particles that are likely to remain suspended for much longer, which could create differences in the injection heights recorded for downwind regions and contribute to the errors. Another minor note is that the radar records data approximately every 6-7 minutes for extended period of time, but the airborne lidar records data continuously for shorter periods of time–the time comparison is not exact, introducing some uncertainty in this comparison. Also important to note is that the grid spacing of ~1000 m within the pre-determined grid could be impacting radar-derived results and that the

radar itself may have outliers and artifacts that contribute to discrepencies in this comparison, adding to the overprediction of heights.

Overall, usage of these retrievals is only recommended in the vicinity of the fire, for which the overall, average percentage difference difference was small (Table 2). Further, to capture the maximum injection heights of a fire with radar retrievals over the whole grid, an appropriate percentile (of the radar-derived heights) would need to be determined. Mean and bias metrics were computed using data from Table 1 using the lidar-derived maximum heights and the 75^{th}-90^{th} percentiles of radar-derived heights, resulting in ~600 m mean error and bias ranging from -2% to 13%. Hence, radar-derived heights within the 75^{th}-90^{th} percentile range would appropriately capture the maximum injection heights, given the >1 km expected resolution at these heights.

One characteristic of the 2019 Williams Flats Fire event was the occurrence of fire-generated thunderstorms (pyro-cumulonimbus or 'pyroCb' for short) around 06 UTC on 8 August 2019 and 00 UTC on 9 August 2019 (Peterson et al., 2022). The DC-8 aircraft flew on 8 August 2019 and sampled the latter pyroCbs. Lidar retrievals for these flights were not included in the analysis given that the aircraft sampled smoke and anvils mostly downwind of the pre-determined grid, primarily due to safety issues. However, the radar-derived heights can be compared to the anvil heights derived in Ye et al., (2021), which are between 9-10 km during 00-03 UTC on 9 August 2019. Shown in Figure 3, the maximum heights for this temporal range are ~13 km, showing a similar overprediction as the other days. However, the heights in the 75^{th}-90^{th} percentiles are within the 5-8 km range, below the maximum injection heights. Thus, a larger percentile may need to be used to better capture the top injection heights for pyroCbs.

4 Conclusions

We have shown that it is possible to fully resolve the diurnal and day-to-day behavior of wildfires using WSR-88D dual polarization data to estimate the injection heights of smoke plumes using BBD as a surrogate for smoke aerosol particles around the source of the fire. The injection height estimation algorithm, which was constructed with the help of previous observations of polarimetric data characteristic to smoke plumes (i.e., Reflectivity $\boldsymbol{Z \geq 10}$ dBZ and correlation coefficient $\boldsymbol{0.2 < C.C. < 0.9}$), was able to estimate the injection heights of BBD

at regular time intervals for the whole life-span of a fire. These extended time series of injection heights derived from the radar data depicted a strong diurnal variability of injection heights, with the deepest smoke injection during the latter half of the day.

To validate the injection height estimation algorithm, the derived injection heights were compared to injection height retrievals from airborne lidar data. For a given time, the radar data was used to retrieve the maximum injection heights within the pre-determined grid whereas the lidar data was retrieved along the flight path. Results indicate that that statistical metrics such as the mean, median, 75^{th} percentile, and 90^{th} percentile heights were well captured (350-820 m mean error). However, the maximum injection heights were consistently over predicted (40% on average) likely due to outliers resulting from the coarsening of the radar vertical resolution with higher altitude. Reflectivity profiles were plotted over time according to the flight path of the aircraft; these location-specific injection height retrievals within the vicinity of the fire yielded better results for maximum injection heights but similar errors for other metrics. Results show that the true maximum smoke injection heights are generally correspond to the radar heights between the 75^{th} and 90^{th} percentile, except for pyroCbs for which a larger percentile value may need to be determined.

While radars allow for the retrieval of real-time smoke injection measurements and for the analyses of the diurnal behavior of smoke plumes, several sources of uncertainty persist. Location-specific comparisons of injection heights derived from both radar and lidar data seem to indicate that as distance from the source of the fire increases, the accuracy of the injection heights (estimated form the radar data) decreases. Further work may involve combining data from several Doppler Radars and accounting for how debris particles are likely to behave when suspended in the atmosphere using numerical models. Another source of uncertainty would be whether the reflectivity and correlation coefficient thresholds are optimal for the accurate estimation of injection heights. Currently, these values have been chosen using prior observations of polarimetric data, however since reflectivity and correlation coefficient values vary from fire to fire, other classifiers need to be explored. Future work will also need to

evaluate the skill of estimating injections from radar data against other methods of estimating injection heights, such as those from satellites that use passive remote sensing.

While having inherent uncertainties, the close to full-time coverage of radar-derived smoke injection heights from operational weather radars has strong potential to help monitor the conditions of fires in a real-time manner. Additionally, it can be used in a variety of applications including the evaluation of smoke injection approacjes in the context of air quality and atmospheric composition modeling (Thapa et al., 2022; Ye et al., 2021), supporting the identification of pyroconvection (Peterson et al., 2022), and assessing historical trends of smoke injection (Wilmot et al., 2022).

Acknowledgments

The authors declare that they have no conflict of interest.

This work has been supported by the following grants: NSF 2013461, NSF 2238338, NASA 80NSSC18K0629, NOAA NA18OAR4310107.

Open Research

NOAA Next Generation Radar (NEXRAD) Level II data that can be accessed in the NOAA National Centers for Environmental Information repository (NOAA National Weather Service (NWS) Radar Operations Center, 1991), was used in the algorithm described in this manuscript. Also used within the algorithm to process and interpret the WSR-88D data, is the Python ARM Radar Toolkit, Py-ART version 1.11.6 (Helmus & Collis, 2016).

The FIREX-AQ data, used to evaluate the results of the algorithm described in the manuscript, is archived by the National Aeronautics and Space Administration, U.S. Government (NASA/LARC/SD/ASDC, 2020). GOES-17 satellite imagery (used in some figures) is also available in the FIREX-AQ repository.

The code for the algorithm, figures, tables, and data analysis are written in Python (Python version 3.9.7), available under the license https://www.python.org and MATLAB version R2020b (The MathWorks Inc., 2020), available at https://www.mathworks.com. The Python code is written with the help of several libraries, including NumPy version 1.21.2 (Harris et al., 2020) under the license https://numpy.org, Matplotlib version 3.4.3 (Hunter, 2007) under the license https://www.matplotlib.org, SciPy version 1.2.1 (Virtanen et al., 2020) under the

license https://scipy.org, and Pandas version 1.2.5 (McKinney, 2010; The pandas development team, 2021) under the license https://pandas.pydata.org. Some figures were also made with the help of Microsoft PowerPoint version 16.75 (Microsoft Corporation, 2023), Keynote version 13.1 (Apple Inc, 2023), and Adobe Illustrator 2023 version 27.4.1 (Adobe Inc., 2023). Code associated with this manuscript is published on GitHub (https://github.com/mansakrishna23/Injection_Height_Estimation_Algorithm) and Zenodo (https://doi.org/10.5281/zenodo.8306303).

References

Adobe Inc. (2023). Adobe Illustrator 2023 (Version 27.4.1). Retrieved from https://www.adobe.com/products/illustrator.html

Amiridis, V., Giannakaki, E., Balis, D. S., Gerasopoulos, E., Pytharoulis, I., Zanis, P., et al. (2010). Smoke injection heights from agricultural burning in Eastern Europe as seen by CALIPSO. *Atmospheric Chemistry and Physics*, *10*(23), 11567–11576. https://doi.org/10.5194/acp-10-11567-2010

Apple Inc. (2023). Keynote (Version 13.1). Retrieved from https://www.apple.com/keynote

Balmes, J. R. (2020). The Changing Nature of Wildfires: Impacts on the Health of the Public. *Clinics in Chest Medicine*, *41*(4), 771–776. https://doi.org/10.1016/j.ccm.2020.08.006

Banta, R. M., Olivier, L. D., Holloway, E. T., Kropfli, R. A., Bartram, B. W., Cupp, R. E., & Post, M. J. (1992). Smoke-Column Observations from Two Forest Fires Using Doppler Lidar and Doppler Radar. *Journal of Applied Meteorology and Climatology*, *31*(11), 1328–1349. https://doi.org/10.1175/1520-0450(1992)031<1328:SCOFTF>2.0.CO;2

Buchholz, R. R., Park, M., Worden, H. M., Tang, W., Edwards, D. P., Gaubert, B., et al. (2022). New seasonal pattern of pollution emerges from changing North American wildfires. *Nature Communications*, *13*(1), 2043. https://doi.org/10.1038/s41467-022-29623-8

Carr, J. L., Wu, D. L., Daniels, J., Friberg, M. D., Bresky, W., & Madani, H. (2020). GEO–GEO Stereo-Tracking of Atmospheric Motion Vectors (AMVs) from the Geostationary Ring. *Remote Sensing*, *12*(22), 3779. https://doi.org/10.3390/rs12223779

Chen, X., Wang, J., Xu, X., Zhou, M., Zhang, H., Castro Garcia, L., et al. (2021). First retrieval of absorbing aerosol height over dark target using TROPOMI oxygen B band: Algorithm development and application for surface particulate matter estimates. *Remote Sensing of Environment*, *265*, 112674. https://doi.org/10.1016/j.rse.2021.112674

Crum, T. D., & Alberty, R. L. (1993). The WSR-88D and the WSR-88D Operational Support Facility. *Bulletin of the American Meteorological Society*, *74*(9), 1669–1688. https://doi.org/10.1175/1520-0477(1993)074<1669:TWATWO>2.0.CO;2

Deb, P., Moradkhani, H., Abbaszadeh, P., Kiem, A. S., Engstrom, J., Keellings, D., & Sharma, A. (2020). Causes of the Widespread 2019-2020 Australian Bushfire Season. *Earth's Future*, *8*(11). https://doi.org/10.1029/2020EF001671

Donald Burgess & Peter S. Ray. (1986). Principles of Radar. In *Mesoscale Meteorology and Forecasting* (pp. 85–117).

Doviak, R. J., Bringi, V., Ryzhkov, A., Zahrai, A., & Zrnić, D. (2000). Considerations for Polarimetric Upgrades to Operational WSR-88D Radars. *Journal of Atmospheric and Oceanic Technology*, *17*(3), 257–278. https://doi.org/10.1175/1520-0426(2000)017<0257:CFPUTO>2.0.CO;2

Gakidou, E., Afshin, A., Abajobir, A. A., Abate, K. H., Abbafati, C., Abbas, K. M., et al. (2017). Global, regional, and national comparative risk assessment of 84 behavioural, environmental and occupational, and metabolic risks or clusters of risks, 1990–2016: a systematic analysis for the Global Burden of Disease Study 2016. *The Lancet*, *390*(10100), 1345–1422. https://doi.org/10.1016/S0140-6736(17)32366-8

Hair, J., Hostetler, C., Cook, A., Harper, D., Notari, A., Fenn, M., et al. (2018). New capability for ozone dial profiling measurements in the troposphere and lower stratosphere from aircraft. *EPJ Web of Conferences*, *176*, 01006. https://doi.org/10.1051/epjconf/201817601006

Harris, C. R., Millman, K. J., van der Walt, S. J., Gommers, R., Virtanen, P., Cournapeau, D., et al. (2020). Array programming with NumPy. *Nature*, *585*(7825), 357–362. https://doi.org/10.1038/s41586-020-2649-2

Hasler, A. F. (1981). Stereographic Observations from Geosynchronous Satellites: An Important New Tool for the Atmospheric Sciences. *Bulletin of the American Meteorological Society*, *62*(2), 194–212. https://doi.org/10.1175/1520-0477(1981)062<0194:SOFGSA>2.0.CO;2

Helmus, J., & Collis, S. (2016). The Python ARM Radar Toolkit (Py-ART), a Library for Working with Weather Radar Data in the Python Programming Language. *Journal of Open Research Software*, *4*(1), e25. https://doi.org/10.5334/jors.119

Higuera, P. E., & Abatzoglou, J. T. (2021). Record-setting climate enabled the extraordinary 2020 fire season in the western United States. *Global Change Biology*, *27*(1), 1–2. https://doi.org/10.1111/gcb.15388

Holleman, I., Huuskonen, A., & Taylor, B. (2022). Solar Monitoring of the NEXRAD WSR-88D Network Using Operational Scan Data. *Journal of Atmospheric and Oceanic Technology*, *39*(2), 193–205. https://doi.org/10.1175/JTECH-D-20-0204.1

Hsu, N. C., Lee, J., Sayer, A. M., Kim, W., Bettenhausen, C., & Tsay, S.-C. (2019). VIIRS Deep Blue Aerosol Products Over Land: Extending the EOS Long-Term Aerosol Data Records. *Journal of Geophysical Research: Atmospheres*, *124*(7), 4026–4053. https://doi.org/10.1029/2018JD029688

Hung, W.-T., Lu, C.-H. (Sarah), Shrestha, B., Lin, H.-C., Lin, C.-A., Grogan, D., et al. (2020). The impacts of transported wildfire smoke aerosols on surface air quality in New York State: A case study in summer 2018. *Atmospheric Environment*, *227*, 117415. https://doi.org/10.1016/j.atmosenv.2020.117415

Hunter, J. D. (2007). Matplotlib: A 2D Graphics Environment. *Computing in Science & Engineering*, *9*(3), 90–95. https://doi.org/10.1109/MCSE.2007.55

Jones, T. A., & Christopher, S. A. (2009). Injection Heights of Biomass Burning Debris Estimated From WSR-88D Radar Observations. *IEEE Transactions on Geoscience and Remote Sensing*, *47*(8), 2599–2605. https://doi.org/10.1109/TGRS.2009.2014225

Kingfield, D. M., & French, M. M. (2022). The Influence of WSR-88D Intra-Volume Scanning Strategies on Thunderstorm Observations and Warnings in the Dual-Polarization Radar Era: 2011–20. *Weather and Forecasting*, *37*(2), 283–301. https://doi.org/10.1175/WAF-D-21-0127.1

Kingsmill, D. E., French, J. R., & Lareau, N. P. (2023). In situ microphysics observations of intense pyroconvection from a large wildfire. *Atmospheric Chemistry and Physics*, *23*(1), 1–21. https://doi.org/10.5194/acp-23-1-2023

Lang, T. J., Rutledge, S. A., Dolan, B., Krehbiel, P., Rison, W., & Lindsey, D. T. (2014). Lightning in Wildfire Smoke Plumes Observed in Colorado during Summer 2012. *Monthly Weather Review*, *142*(2), 489–507. https://doi.org/10.1175/MWR-D-13-00184.1

Lee, J., Hsu, N. C., Bettenhausen, C., Sayer, A. M., Seftor, C. J., & Jeong, M.-J. (2015). Retrieving the height of smoke and dust aerosols by synergistic use of VIIRS, OMPS, and CALIOP observations. *Journal of Geophysical Research: Atmospheres*, *120*(16), 8372–8388. https://doi.org/10.1002/2015JD023567

Liu, H., & Chandrasekar, V. (2000). Classification of Hydrometeors Based on Polarimetric Radar Measurements: Development of Fuzzy Logic and Neuro-Fuzzy Systems, and In Situ Verification. *Journal of Atmospheric and Oceanic Technology*, *17*(2), 140–164. https://doi.org/10.1175/1520-0426(2000)017<0140:COHBOP>2.0.CO;2

Loría-Salazar, S. M., Sayer, A. M., Barnes, J., Huang, J., Flynn, C., Lareau, N., et al. (2021). Evaluation of Novel NASA Moderate Resolution Imaging Spectroradiometer and Visible Infrared Imaging Radiometer Suite Aerosol Products and Assessment of Smoke Height Boundary Layer Ratio During Extreme Smoke Events in the Western USA. *Journal of Geophysical Research: Atmospheres*, *126*(11). https://doi.org/10.1029/2020JD034180

Manisalidis, I., Stavropoulou, E., Stavropoulos, A., & Bezirtzoglou, E. (2020). Environmental and Health Impacts of Air Pollution: A Review. *Frontiers in Public Health*, *8*, 14. https://doi.org/10.3389/fpubh.2020.00014

McCarthy, N., Guyot, A., Dowdy, A., & McGowan, H. (2019). Wildfire and Weather Radar: A Review. *Journal of Geophysical Research: Atmospheres*, *124*(1), 266–286. https://doi.org/10.1029/2018JD029285

McKinney, W. (2010). Data Structures for Statistical Computing in Python (Vol. 445, pp. 56–61). Presented at the Python in Science Conference, Austin, Texas. https://doi.org/10.25080/Majora-92bf1922-00a

Melnikov, V. M., Zrnic, D. S., Rabin, R. M., & Zhang, P. (2008). Radar polarimetric signatures of fire plumes in Oklahoma. *Geophysical Research Letters*, *35*(14). https://doi.org/10.1029/2008GL034311

Michailidis, K., Koukouli, M.-E., Balis, D., Veefkind, P., de Graaf, M., Mona, L., et al. (2022). Validation of the TROPOMI/S5P Aerosol Layer Height using EARLINET lidars. *Atmospheric Chemistry and Physics Discussions*, 1–30. https://doi.org/10.5194/acp-2022-412

Microsoft Corporation. (2023). Microsoft PowerPoint (Version 16.75). Retrieved from https://office.microsoft.com/PowerPoint

NASA/LARC/SD/ASDC. (2020). FIREX-AQ DC-8 In-Situ Aerosol Data [Data set]. NASA Langley Atmospheric Science Data Center DAAC. Retrieved from https://doi.org/10.5067/ASDC/FIREXAQ_Aerosol_AircraftInSitu_DC8_Data_1

National Research Council. (2002). *Weather Radar Technology Beyond NEXRAD*. The National Academies Press. https://doi.org/10.17226/10394

NOAA National Weather Service, National Weather Service, & US Department of Commerce. (2023, April 3). JetStream Max: Volume Coverage Patterns (VCPs). Retrieved January 17, 2023, from https://www.weather.gov/jetstream/vcp_max

NOAA National Weather Service (NWS) Radar Operations Center. (1991). NOAA Next Generation Radar (NEXRAD) Level 2 Base Data. [Data set]. https://doi.org/doi:10.7289/V5W9574V

Peterson, D. A., Thapa, L. H., Saide, P. E., Soja, A. J., Gargulinski, E. M., Hyer, E. J., et al. (2022). Measurements from inside a Thunderstorm Driven by Wildfire: The 2019 FIREX-AQ Field Experiment. *Bulletin of the American Meteorological Society*, *103*(9), E2140–E2167. https://doi.org/10.1175/BAMS-D-21-0049.1

Rodriguez, B., Lareau, N. P., Kingsmill, D. E., & Clements, C. B. (2020). Extreme Pyroconvective Updrafts During a Megafire. *Geophysical Research Letters*, *47*(18), e2020GL089001. https://doi.org/10.1029/2020GL089001

Sayer, A. M., Hsu, N. C., Lee, J., Kim, W. V., & Dutcher, S. T. (2019). Validation, Stability, and Consistency of MODIS Collection 6.1 and VIIRS Version 1 Deep Blue Aerosol Data Over Land. *Journal of Geophysical Research: Atmospheres*, *124*(8), 4658–4688. https://doi.org/10.1029/2018JD029598

Schum, S. K., Zhang, B., Džepina, K., Fialho, P., Mazzoleni, C., & Mazzoleni, L. R. (2018). Molecular and physical characteristics of aerosol at a remote free troposphere site: implications for atmospheric aging. *Atmospheric Chemistry and Physics*, *18*(19), 14017–14036. https://doi.org/10.5194/acp-18-14017-2018

Shamsaei, K., Juliano, T. W., Roberts, M., Ebrahimian, H., Lareau, N. P., Rowell, E., & Kosovic, B. (2023). The Role of Fuel Characteristics and Heat Release Formulations in Coupled Fire-Atmosphere Simulation. *Fire*, *6*(7), 264. https://doi.org/10.3390/fire6070264

Thapa, L. H., Ye, X., Hair, J. W., Fenn, M. A., Shingler, T., Kondragunta, S., et al. (2022). Heat flux assumptions contribute to overestimation of wildfire smoke injection into the free troposphere. *Communications Earth & Environment*, *3*(1), 1–11. https://doi.org/10.1038/s43247-022-00563-x

The MathWorks Inc. (2020). MATLAB version: 9.9 (R2020b). Natick, Massachusetts, United States. Retrieved from https://www.mathworks.com

The pandas development team. (2021, June). pandas-dev/pandas: Pandas 1.2.5 (Version 1.2.5). https://doi.org/10.5281/zenodo.5013202

Thurston, W., Kepert, J. D., Tory, K. J., Fawcett, R. J. B., Thurston, W., Kepert, J. D., et al. (2017). The contribution of turbulent plume dynamics to long-range spotting. *International Journal of Wildland Fire*, *26*(4), 317–330. https://doi.org/10.1071/WF16142

Tory, K. J., Thurston, W., & Kepert, J. D. (2018). Thermodynamics of Pyrocumulus: A Conceptual Study. *Monthly Weather Review*, *146*(8), 2579–2598. https://doi.org/10.1175/MWR-D-17-0377.1

Val Martin, M., Logan, J. A., Kahn, R. A., Leung, F.-Y., Nelson, D. L., & Diner, D. J. (2010). Smoke injection heights from fires in North America: analysis of 5 years of satellite observations. *Atmospheric Chemistry and Physics*, *10*(4), 1491–1510. https://doi.org/10.5194/acp-10-1491-2010

Val Martin, Maria, Kahn, R. A., & Tosca, M. G. (2018). A Global Analysis of Wildfire Smoke Injection Heights Derived from Space-Based Multi-Angle Imaging. *Remote Sensing*, *10*(10), 1609. https://doi.org/10.3390/rs10101609

Veefkind, J. P., Aben, I., McMullan, K., Förster, H., de Vries, J., Otter, G., et al. (2012). TROPOMI on the ESA Sentinel-5 Precursor: A GMES mission for global observations of the atmospheric composition for climate, air quality and ozone layer applications. *Remote Sensing of Environment*, *120*, 70–83. https://doi.org/10.1016/j.rse.2011.09.027

Virtanen, P., Gommers, R., Oliphant, T. E., Haberland, M., Reddy, T., Cournapeau, D., et al. (2020). SciPy 1.0: fundamental algorithms for scientific computing in Python. *Nature Methods*, *17*(3), 261–272. https://doi.org/10.1038/s41592-019-0686-2

Warneke, C., Schwarz, J. P., Dibb, J., Kalashnikova, O., Frost, G., Al-Saad, J., et al. (2023). Fire Influence on Regional to Global Environments and Air Quality (FIREX-AQ). *Journal of Geophysical Research: Atmospheres*, *128*(2), e2022JD037758. https://doi.org/10.1029/2022JD037758

Wilmot, T. Y., Mallia, D. V., Hallar, A. G., & Lin, J. C. (2022). Wildfire plumes in the Western US are reaching greater heights and injecting more aerosols aloft as wildfire activity intensifies. *Scientific Reports*, *12*(1), 12400. https://doi.org/10.1038/s41598-022-16607-3

Winker, D. M., Hunt, W. H., & Hostetler, C. A. (2004). Status and performance of the CALIOP lidar. In *Laser Radar Techniques for Atmospheric Sensing* (Vol. 5575, pp. 8–15). SPIE. https://doi.org/10.1117/12.571955

Ye, X., Arab, P., Ahmadov, R., James, E., Grell, G. A., Pierce, B., et al. (2021). Evaluation and intercomparison of wildfire smoke forecasts from multiple modeling systems for the 2019 Williams Flats fire. *Atmospheric Chemistry and Physics*, *21*(18), 14427–14469. https://doi.org/10.5194/acp-21-14427-2021

Ye, X., Saide, P. E., Hair, J., Fenn, M., Shingler, T., Soja, A., et al. (2022). Assessing Vertical Allocation of Wildfire Smoke Emissions Using Observational Constraints From Airborne Lidar in the Western U.S. *Journal of Geophysical Research: Atmospheres*, *127*(21), e2022JD036808. https://doi.org/10.1029/2022JD036808

Zrnic, D., Zhang, P., Melnikov, V., & Mirkovic, D. (2020). Of Fire and Smoke Plumes, Polarimetric Radar Characteristics. *Atmosphere*, *11*, 363. https://doi.org/10.3390/atmos11040363